Res. Chem. Intermed. Vol. 20, No. 8, pp. 783-806 (1994)

SILVER CLUSTERS IN THE CAGES OF ZEOLITES: A QUANTUM CHEMICAL STUDY

M. BRÄNDLE AND G. CALZAFERRI*
Institute for Inorganic and Physical Chemistry, University of Berne, CH-3000 Bern 9, Switzerland

Received 24 September 1993; accepted 8 November 1993

Abstract--The electronic structure of zeolite A is developed in a step by step procedure from the simple O_h-$H_8Si_8O_{12}$ molecule, to the $^1_\infty[(\text{-O})_2H_4(Si_8O_{12})]$ chain, to the $^2_\infty[(\text{-O})_4(Si_8O_{12})]$ layer, and finally to the silica zeolite A framework $^3_\infty[Si_{24}O_{48}]$. It is remarkable how well the calculated band structures of both, $^2_\infty[(\text{-O})_4(Si_8O_{12})]$ and $^3_\infty[Si_{24}O_{48}]$ correspond to the experimentally determined band structure of α-quartz with a Fermi level of -10.55 eV. The HOMO region consists in each case of nonbonding 2p-oxygen bands which in a localized language can be denoted as oxygen lone pairs ($|O<$). We observe in each case the typical behaviour of an insulator with saturated valencies whose electronic structure can be described as being localized and is already present in the starting O_h-$H_8Si_8O_{12}$ molecule. The double-8-rings D8R of the $^2_\infty[(\text{-O})_4(Si_8O_{12})]$ layer have a pore diameter of 4.1 Å, the same as the pore opening of zeolite A. It is large enough to accept up to four Ag, forming $^2_\infty[(\text{-O})_4(Si_8O_{12})Ag_n]$, n = 1, 2, 3, 4, layers, suitable for modelling the electronic interactions between the zeolite cavity embedded silver clusters and between the clusters and the zeolite framework. With one Ag per D8R the band structure is simply a superposition of the 4d, 5s and 5p levels of a layer of nearly noninteracting Ag and the silicon dioxide layer. The Ag-d band lies below the oxygen lone pairs, the Ag-s band lies about 3 eV above the oxygen lone pairs, and the Ag-5p bands are in the antibonding silicon dioxide region. The first electronic transition is of oxygen lone pair to Ag-5s LMCT type. Increasing silver content results in progressive splitting of the 5σ Ag bands and shifts the first $(Ag^{m+}_n)^\bullet \leftarrow (|O<)$ charge transfer transition to lower energies. The filled Ag 4d-bands lie always significantly below the ($|O<$) HOCOs (highest occupied crystal orbitals) but their band width increases with increasing silver content. In all cases the zeolite environment separates the Ag clusters through antibonding Ag-($|O<$) interactions so that the coupling remains weak and it makes sense to describe the Ag clusters in the D8R as quantum dots weakly interacting with each other.

INTRODUCTION

Zeolite supported silver micro structures have been prepared by treating Ag^+-exchanged zeolites with H_2 or CO [1,2], with metal vapours [3], by heating [4], by photochemical reduction [5,6], and, very recently, by electrochemical reduction on zeolite-monograin modified electrodes [7]. Similarly sized silver clusters have also been formed by pulse radiolysis [8,9], in the free molecular beam [10], and from trapped beam in rare gas matrices [11]. Possible applications of silver clusters embedded in zeolites, ranging from catalysis, nonlinear optics, optical computing, quantum electronics, to photochemical energy

storing devices, have been discussed [12,13].

Our particular interest has focussed on the photoreaction of silver exchanged zeolite A with water as a reducing agent, whereby molecular oxygen is liberated from water at neutral pH [14]. The shift of the spectral sensitivity in the early stage of this reaction reveals that a self-sensitization process takes place. It is ascribed to a quantum size effect in which during the photoreaction chromophores are produced with a bathochromically shifted absorption. The size of the silver clusters involved is confined by the zeolite cavities [6]. Investigations of this photoreaction's applicability in an energy storage device [13,15] benefit from supporting results of *e.g.* detailed x-ray structure determinations, measurements of redox and ionization potentials, infrared, Raman, UV/VIS, and luminescence spectroscopy, and EPR studies. As an example Kim and Seff have resolved octahedral Ag_6 clusters in the α- and in the β-cage of zeolite A by single crystal x-ray diffraction [3,16,17] which according to their description are stabilized by surrounding cations, *eg.* Ag^+ or Rb^+, and charged Ag_2, Ag_3, and the $Ag_6{\bullet}(Ag^+)_8$ cluster have been observed by EPR spectroscopy [18,19].

In preceding studies we have explained that the electronic transition responsible for the longest wavelength absorption of a previously unexposed silver zeolite is of LMCT type, exciting an oxygen lone pair electron into the empty 5s orbital of Ag^+. To further develop our understanding, one can start by discussing the electronic structure of isolated Ag^+ ions in the neighbourhood of zeolite-oxygen lone pairs and study their interaction with light. A simplified way to illustrate this is shown in Figure 1. We already know that there is no indication that the HOMO region of an alkali ion zeolite develops as valence band or the LUMO region as conduction band. The HOMO region of the alkali ion zeolite framework consists of many closely spaced localized states strongly concentrated on the

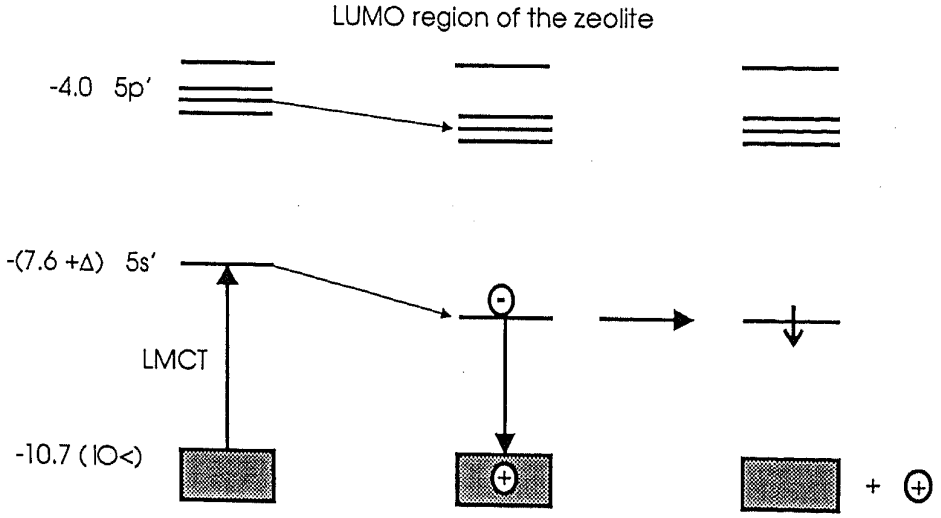

Figure 1. Development of the energy diagram in eV of an isolated Ag^+ in the zeolite framework. The splitting of the 5p' levels is not shown. Some of the 5p' levels may reach into the LUMO region of the zeolite. The zeolite oxygen lone pair region is denoted as (|O<). It consists of closely spaced localized states. In this scheme Δ has a negative value because of the antibonding interaction of the Ag 5s orbitals with the oxygen lone pairs.

oxygen atoms [20]. We call this region lone pair oxygen region of the zeolite and denote it as (| O<). The energy of the edge of the (| O<) levels is close to -10.7 eV as we know from our studies on $H_8Si_8O_{12}$ [21]. The LUMO region consists of localized states. 5s and 5p denote the orbitals of the free silver atom while 5s′ and 5p′ are those of Ag in the zeolite. The position of the 5s′ level and the 5p′ levels can be estimated from the first ionization potential of Ag^0, which is 7.6 eV, and from the energy difference $E_{Ag}(4d^{10}5p^1)$-$E_{Ag}(4d^{10}5s^1)$ which is 3.74 eV. The 5s′ level is shifted by Δ to higher energy because of antibonding interactions of the 5s orbital with the oxygen lone pairs of the zeolite. The 5p′ levels split to some extent, depending on the symmetry of the environment. This situation is illustrated on the left side of Figure 1. Because of the large energy difference between the 5s and the 5p levels, we expect a rather pure zeolite oxygen to 5s′ ligand to metal charge transfer (LMCT) absorption. It seems reasonable to assume that the LMCT blows up the silver which has to change its position by about 0.2 Å, because the ionic radius of Ag^+ is about 1.26 Å while the radius of Ag^0 is of the order of 1.45 Å. As a consequence, the 5s′ level relaxes to a configuration of lower energy denoted as $(| O<)^{\oplus} (5s')^1$. This state can relax to the ground state by emitting a photon with a large Stokes shift. Such luminescence has been reported [22,23]. Its interpretation, however, should be reinvestigated in view of our results. Thermal relaxation is another channel of deactivation and, more interestingly, the hole $(| O<)^{\oplus}$ can diffuse away, probably to the surface of the zeolite particles, and eventually induce an oxidation reaction. If this latter process is efficient, enough positive charge can accumulate so that water oxidation takes place. The ground state of the system is a singlet S_O denoted as $(| O<)(5s')^0$. The first excited state configuration is denoted as $(| O<)^{\oplus}(5s')^1$ and the first relaxed excited state configuration as $(—O<)^{\oplus}(5s')^1_{relaxed}$.

We have recently discussed consequences of the electronic structure of isolated silver clusters placed into the zeolite framework [13], and some results are summarized in Figure 2 where we show how the silver metal-electrode potential $E^0_{Ag+(aq)/Agn}$ of the reaction $Ag_{n-1} + Ag^+ + e \rightarrow Ag_n$ [24] and the HOMO/LUMO energies change from Ag to Ag_2, D_{2h}-Ag_4, O_h-Ag_6 and finally to Ag_∞. The redox potential drops accordingly from -1.8 V for Ag to 0 V for Ag_{19} and reaches 0.8 V for bulk silver. The ionization potential $Ip(Ag_n)$ is reflected by the HOMO. The energy of the HOMO raises with increasing cluster size. The behaviour of the LUMO, however, is more complicated and the development of the light absorption probability is not uniform. Furthermore electronic transitions of the following type have to be considered: $(Ag^{m+}_n)^{\bullet} \leftarrow (| O<)$, $(Ag^{m+}_n)^{\bullet} \leftarrow (Ag^{m+}_n)$ and in strongly reduced samples perhaps also zeolite (LUMO) $\leftarrow (Ag^{m+}_n)$.

The interaction of the zeolite framework with the silver species is not taken into account in Figure 2. The data are, however, sufficient to conclude that the usual quantum size energy level diagrams and the properties of naked clusters are not sufficient to describe the behaviour of the system. Furthermore we know very little about the interactions between clusters in the different cages which we expect to be important in charge transport processes within the silver containing zeolite crystals, and we would like to improve our understanding of the experimentally observed self-sensitization, the interactions of the metal atoms and cations within the zeolite framework and the mechanism of the photochemical

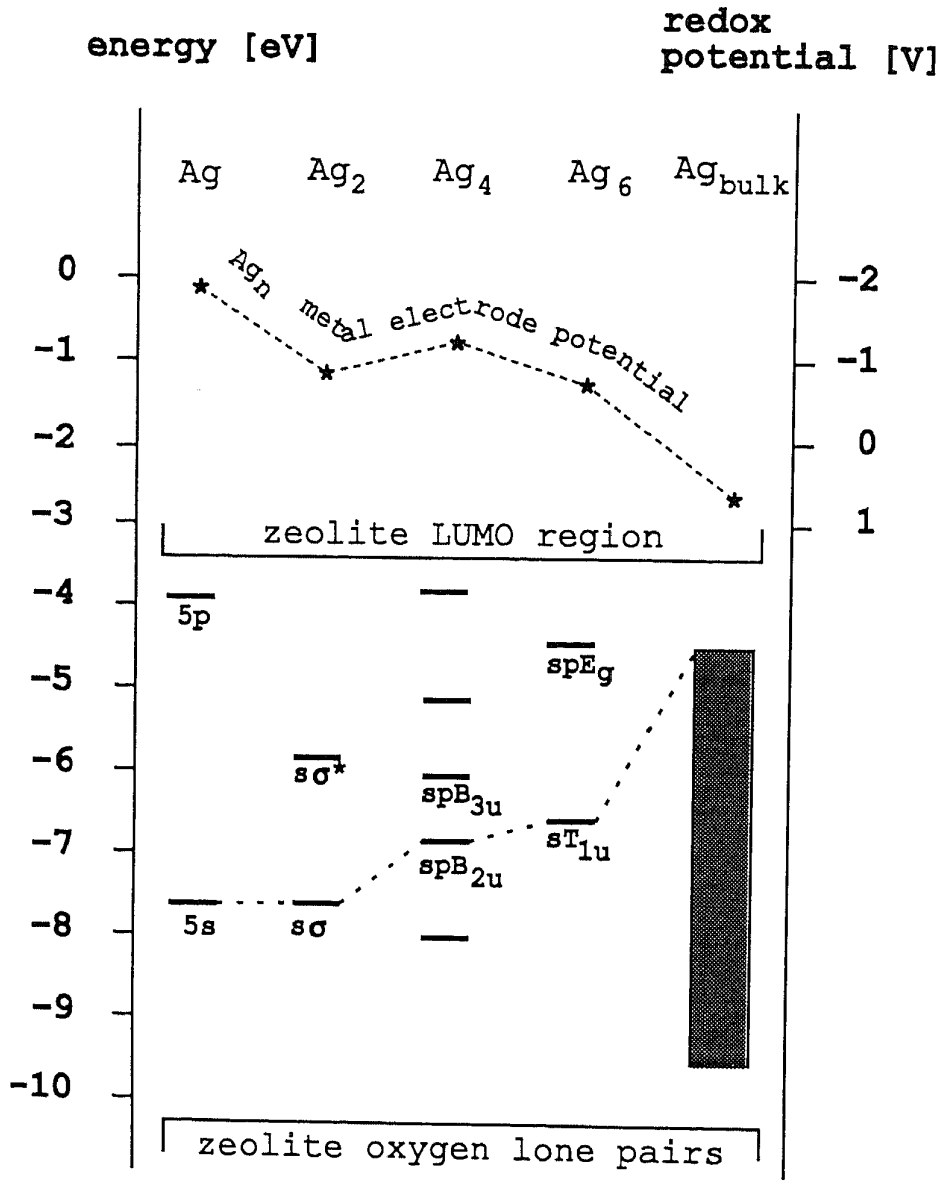

Figure 2. Silver cluster metal electrode potential $E^0_{Ag+(aq)/Agn}$ of the reaction $Ag_{n-1} + Ag^+ + e \rightarrow Ag_n$ and HOMO/LUMO region of the silver clusters in comparison to the HOMO/LUMO orbitals of the zeolite framework. Ag_n orbitals between -10.5 eV and -3.5 eV are shown. The HOMOs of the silver clusters are connected by a dashed line. The number of electrons in the HOMOs are 1, 2, 2 and 4 for Ag, Ag_2, Ag_4 and Ag_6, respectively.

water oxidation.

Computational chemistry gives insight into the electronic structure and interactions of zeolite embedded metal clusters. Zeolites are crystalline and band structure calculations are therefore a possible approach. *Ab initio* and semi-empirical band structure calculations reported in the literature concern mainly silicon dioxide [25-26] and silicates [27-28]. Recently a note on the first periodic Hartree-Fock simulation of electrostatic potentials in

silica-rich sodalite has appeared [29]. While molecular orbital calculations of silver species in different cages have been published [20,30,31], no band structure study on zeolites containing guest molecules is known to the authors.

The unit cell of silver zeolite A is huge and its seems appropriate to proceed step by step from simpler systems to more complex structures. The aluminosilcate framework of zeolite A can be generated by placing cubic double-4-rings, D4R-($Al_4Si_4O_{12}$), in the centres of the edges of a cube of edge 12.4 Å and by connecting the D4R's via oxygen bridges. The centre of the resulting unit cell is a large cavity, denoted as α-cage, with a free diameter of about 11.5 Å. 8-membered rings with a free diameter of 4.1 Å give access to it [32]. The O_h-$H_8Si_8O_{12}$ molecule appears as an excellent model for studying the properties of zeolite A [33], and for generating extended structures to mimic some of its aspects. The interconnection of zeolite A, the D4R and $H_8Si_8O_{12}$ is illustrated in Scheme 1 [34].

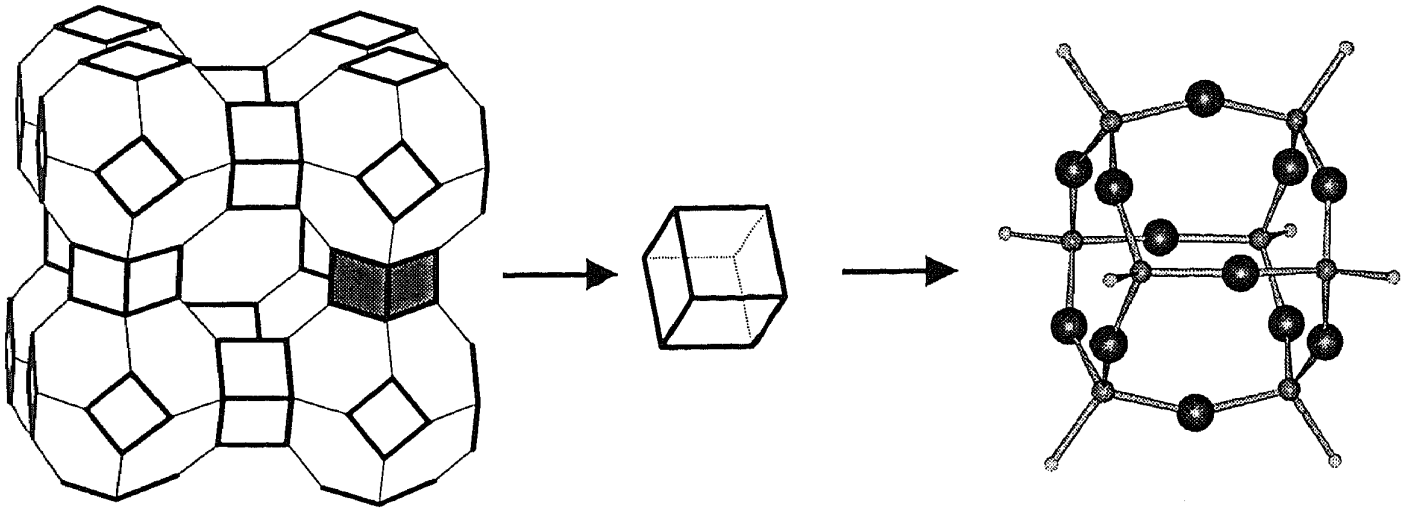

Scheme 1

Relation between the structure of zeolite A, the D4R double-4-ring and the $H_8Si_8O_{12}$ molecule.

Following this line we generate first a linear array based on the Si_8O_{12} structure of $H_8Si_8O_{12}$. We then proceed to a two-dimensional layer, which already includes the 8-membered rings and the corresponding cavities, large enough for silver clusters up to Ag_4. The next step is to extend the structure into three dimensions. We neglect the influence of the negative charges of zeolite A, created by the aluminum according to $[SiO_2)_{12}(AlO_2)_{12}]^{12}$, which are responsible for its ion exchange capability and stability, and we hope that a great part of

the fundamental aspects of the electronic structure of zeolite A is preserved by this procedure which facilitates the calculations and the discussion a lot.

$H_8Si_8O_{12}$ AS MODEL COMPOUND

The $H_{8Si}8O_{12}$ molecule has been shown to be an excellent starting point for quantitatively describing the vibrational structure of zeolite A [34]. Its first ionization potential of -10.7 eV represents the upper edge of the oxygen lone pair orbitals and corresponds closely to the first ionization energy of α-quartz, -10.4 eV, as determined by valence-band photoelectron spectroscopy [35]. The structure of $H_8Si_8O_{12}$ suggests the building of a linear chain, $^1_\infty[(-O)_2H_4(Si_8O_{12})]$, by connecting $H_4Si_8O_{12}$ fragments via oxygen bridges as illustrated in Scheme 2. This chain possesses a three-dimensional structure but is one-dimensional in its periodicity.

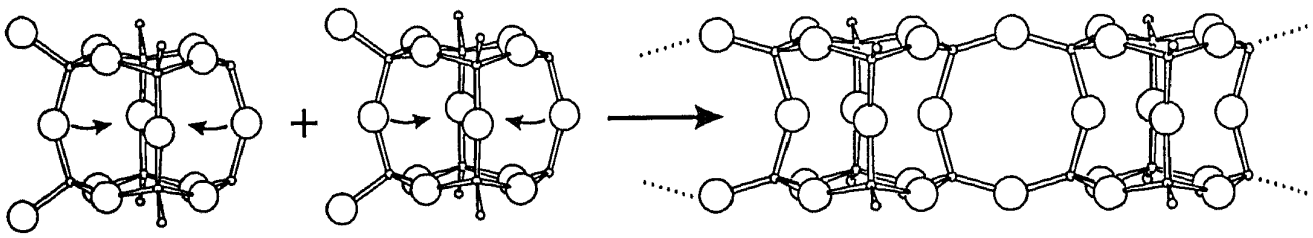

Scheme 2
Linear chain generated by connecting $H_4Si_8O_{12}$ fragments via oxygen bridges.

In the process of building the $^1_\infty[(-O)_2H_4(Si_8O_{12})]$ chain based on the structure of $H_8Si_8O_{12}$ [36] the oxygens of the linking rings come much too close. As a consequence Si-O-Si angles have to be adapted by pulling the corresponding oxygens into the Si_8O_{12}-D4R cages, as indicated by the arrows in Scheme 2, a movement which costs little energy because of the softness of this bending mode [34,36-38]. This change of angles is related to a change of the Si-O bond lengths according to the guidelines given by Gibbs [39], based on EHMO calculations and on experimental data of silicates, which state that the Si-O bond lengths are linearly proportional to the reduced overlap populations and that wide O-Si-O angles result in short Si-O bonds and vice versa. More recently it was found in $H_8Si_8O_{12}$, $H_{10}Si_{10}O_{15}$ and $(CO)_4CoH_7Si_8O_{12}$ that the Si-O distance in Å and the Si-O-Si angle α are related by $d = 1.59 + (180-\alpha)^4 \bullet 2.1 \bullet 10^{-8}$ [38,40], a relation which is expected to hold for the D4R of zeolite A.

We now link the $^1_\infty[(-O)_2H_4(Si_8O_{12})]$ chains by substituting the 4 H atoms by oxygen bridges and we obtain the appealing network $^2_\infty[(-O)_4(Si_8O_{12})]$ in Scheme 3 which possesses a three-dimensional structure but is two-dimensional in its periodicity with a unit cell length

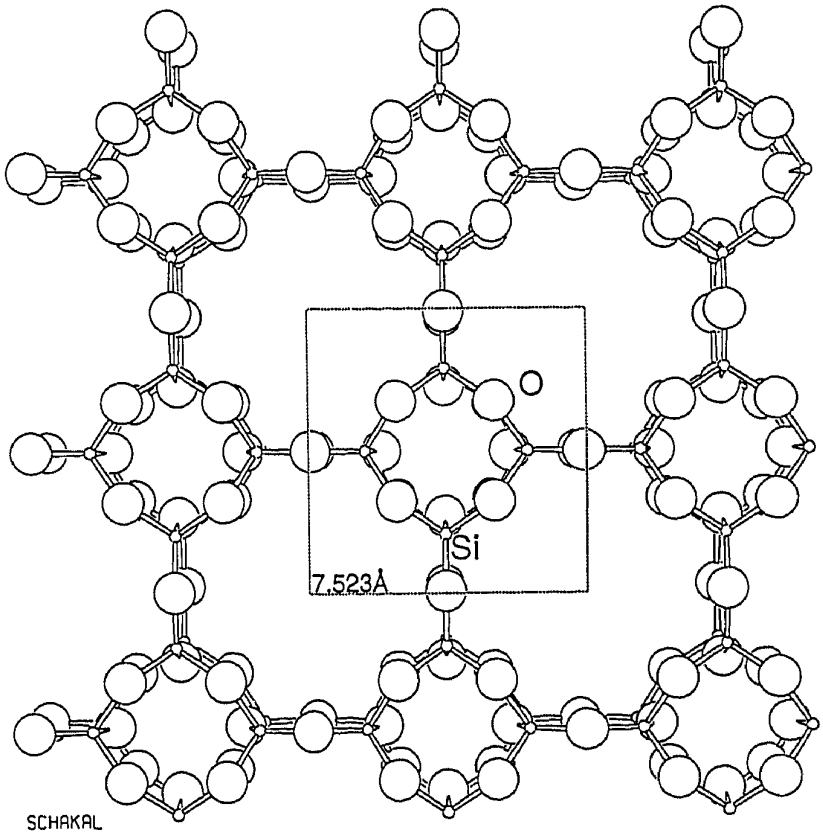

Scheme 3
$^{2}_{\infty}[(-O)_4(Si_8O_{12})]$ layer.

of 7.523 Å. The double-8-rings D8R formed by this procedure have a pore diameter of about 4.1 Å, the same as the 8-ring pore opening of zeolite A or the D8R of zeolite rho [32]. The last step consists in connecting the D4R-Si_8O_{12} cages via oxygen bridges to form the silicon dioxide analogue of zeolite A, $^{3}_{\infty}[Si_{24}O_{48}]$ shown in Scheme 4. This means that the $H_8Si_8O_{12}$ molecule allows in a step by step process to proceed from the molecule to the infinite chain $^{1}_{\infty}[(-O)_2H_4(Si_8O_{12})]$, to the infinite layer $^{2}_{\infty}[(-O)_4(Si_8O_{12})]$, and finally to the infinite three-dimensional $^{3}_{\infty}[Si_{24}O_{48}]$ structure of zeolite A.

COMPUTATIONAL PROCEDURE

Method

Molecular orbital calculations have been performed with the extended-Hückel method [41] in its ASED (atom superposition and electron delocalization) form [42,43] by means of the ICONC QCMP #116 extended-Hückel MO program [44]. Band structure calculations have been carried out with the extended-Hückel tight-binding method [45,46] in its ASED form [47], briefly outlined below.

Given a set of atomic basis functions χ_t for the unit cell, a set of Bloch basis functions $\phi_t(k)$ is formed by constructing Bloch sums over the N cells of the crystal

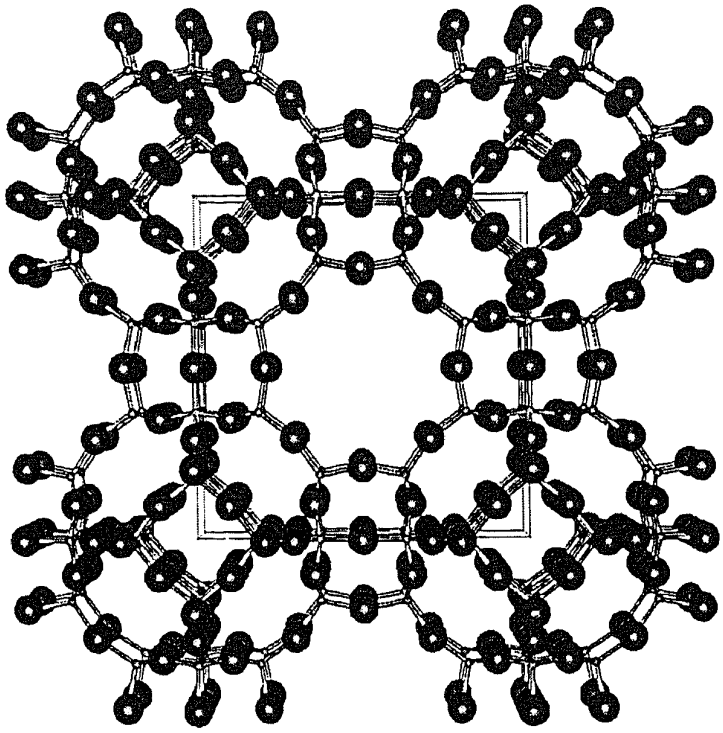

Scheme 4
Structure of zeolite A.

$$\phi_t(k) = N^{-1/2}\sum_t e^{ik\cdot Rt}\chi_t(r - R_t) \quad (1)$$

In this formula R_t is a direct space lattice vector, the wave vector k ranges through the N values of the first *Brillouin* zone and the summation runs over all direct lattice vectors. The LCAO crystal orbitals are given as

$$\Psi_n(k) = \sum_t C_t^n(k)\phi_t(k) \quad (2)$$

where n is the band index. The coefficients $C_t^n(k)$ and energies $\varepsilon^n(k)$ are determined by finding the solutions to the eigenvalue equation

$$[\boldsymbol{H}(k) - E(k)\boldsymbol{S}(k)] \cdot \boldsymbol{C}(k) = 0 \quad (3)$$

where

$$H_{tu}(k) = \langle \phi_t(k) | H | \phi_u(k) \rangle$$
$$S_{tu}(k) = \langle \phi_t(k) | \phi_u(k) \rangle \quad (4)$$

The off-diagonal elements $H_{tu} = \langle \chi_t | H | \chi_u \rangle$ are evaluated by the distance-dependent weighted *Wolfsberg-Helmhotz* formula [42].

$$H_{tu} = 1/2\, K_{tu} S_{tu} (H_{tt} + H_{uu}) \quad . \quad (5)$$

$$K_{tu} = 1 + (K - 1) e^{-\delta(R_{tu} - d_0)} \quad with \quad K = 1 + \kappa + \Delta^2 - \Delta^4 \kappa$$
$$and \quad \Delta = \frac{H_{tt} - H_{uu}}{H_{tt} + H_{uu}} \quad (6)$$

κ and δ are parameters, d_0 is equal to the sum of the orbital radii, calculated from the *Slater* exponents, and R_{tu} denotes the distance between two atoms. The total electronic energy per unit cell is obtained by summation over all occupied energy levels $\varepsilon_n(k)$ and integration over the first *Brillouin* zone BZ with volume V_{BZ} [45].

$$E_{EHMO} = \frac{1}{V_{BZ}} \int_{BZ} 2 \sum_{n}^{occ} \varepsilon^n(k)\, d^3k \quad (7)$$

The total potential energy E_{tot} is calculated in the same way as for molecules by adding an approximate two-body repulsive electrostatic energy term E_{Rep} to the extended-Hückel binding energy ΔE_{EHMO}

$$\Delta E_{EHMO} = E_{EHMO} - \sum_s b_s^0 E_s^0 \quad (8)$$

$$E_{tot}(\boldsymbol{R}) = \Delta E_{EHMO}(\boldsymbol{R}) + E_{Rep}(\boldsymbol{R}) \quad (9)$$

$\sum_s b^0_s E^0_s$ is the sum of atomic valence orbital ionization potentials, each of them times the orbital occupation number b^0_s of the free atoms and **R** is the matrix of the coordinates.

This procedure has been implemented into the extended-Hückel band structure program package EHMACC QCPE #571 [48]; for details see [47].

Parameters

Calculations have been performed with the parameters listed in Table 1. The (3s,3p) *Slater* exponents were determined to match the correct Si-O bond lengths of orthosilicic acid $Si(OH)_4$ and disilic acid $Si_2O_7H_6$ in Scheme 5 [49-51] by applying the same procedure as described in [43] for the water molecule. They are slightly more contracted than those used for $H_8Si_8O_{12}$ which is reasonable because of the change of the silicon oxidation state from Si^{+III} to Si^{+IV}. The oxygen and silver *Slater* exponents were taken from [43] and from [13], respectively. The Si and O valence ionization potentials of $^2_\infty[(\text{-O})_4(Si_8O_{12})]$ were averaged over all resulting values from an EHMO charge iteration calculation on a $(D4R)_4$ fragment, with free valencies saturated by OH groups. Those of $^3_\infty[Si_{24}O_{48}]$ where obtained by applying the same procedure to a $(D4R)_{12}$ fragment, simulating the α-cage, with free valencies saturated by OH groups. Standard parameters $(\kappa,\delta) = (1.0, 0.35\ Å^{-1})$ were used for the off diagonal elements (5), (6) with the exception of Ag-Ag interactions where $\kappa = 0.6$ was used as in earlier calculations on silver clusters [13].

Table 1

Slater parameters and valence coulomb integrals H_{ii} (eV).

Compound	Element	ns	ζ_{ns}	H_{ss}	np	ζ_{np}	H_{pp}	nd	$\zeta_{nd,1}$	C_1	H_{dd}
									$\zeta_{nd,2}$	C_2	
$^2_\infty[(\text{-O})_4(Si_8O_{12})]$	Si	3	1.780	-20.61	3	1.780	-12.50				
	O	2	2.575	-26.25	2	2.275	-10.84				
	Ag[a]	5	1.698	-7.58	5	1.300	-3.83	4	3.912	0.825	-12.77
									1.545	0.329	
	Ag[b]	5	1.85	-6.35	5	1.300	-3.00	4	3.912	0.825	
									1.545	0.329	
$^3_\infty[Si_{24}O_{48}]$	Si	3	1.780	-21.52	3	1.780	-13.30				
	O	2	2.575	-26.84	2	2.275	-11.37				

[a]Used for $^2_\infty[(\text{-O})_4(Si_8O_{12})Ag_n]$, n = 1.

[b]Used for $^2_\infty[(\text{-O})_4(Si_8O_{12})Ag_n]$, n > 1, see [13].

Geometry

The important distances and bond angles for the $^2_\infty[(\text{-O})_4(Si_8O_{12})]$ layer are: α(Si-O-Si) = 148.4°. $\alpha(\text{O-Si-O})_{\text{outer-cage}} = 121.6°$, $\alpha(\text{O-Si-O})_{\text{inner-cage}} = 109.47°$ and 92.1°, respectively, d(Si-

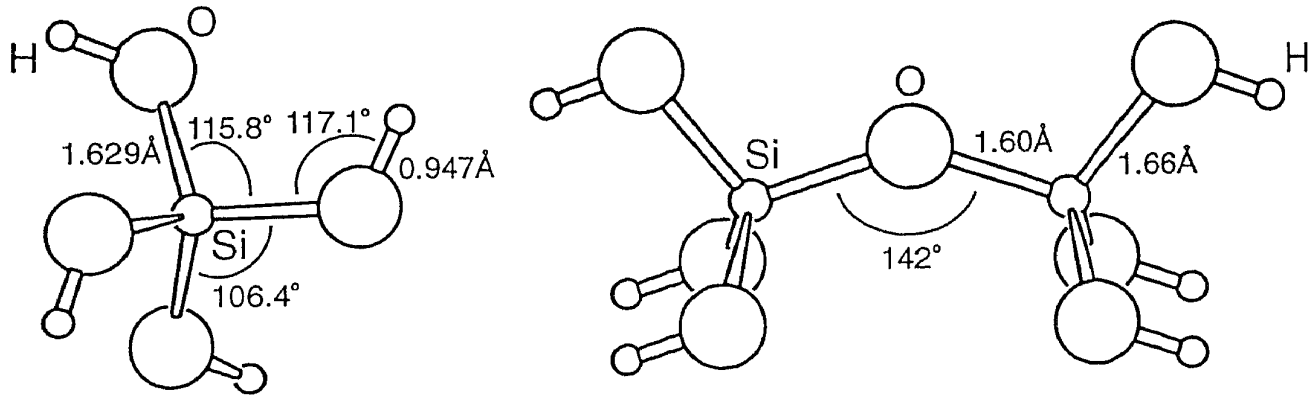

Scheme 5
Structure of $Si(OH)_4$ and $Si_2O_7H_6$.

O_{bridge}) = 1.59 Å, d(Si-O_{cage}) = 1.64 Å. The unit cell length and symmetry are 7.532 Å and p4mm, respectively. The structure of the hypothetical high silica zeolite A $^{3}_{\infty}[Si_{24}O_{48}]$ has been estimated from the experimental crystal structure of silica-sodalite [52-53]. A lattice constant of 11.954 Å results for the simple cubic Pm3m structure of the silica zeolite A with d(Si-O) = 1.587 Å and α(Si-O-Si) = 159.7°.

Band Structure

Band structure diagrams of $^{2}_{\infty}[(-O)_4(Si_8O_{12})]$ and of $^{2}_{\infty}[(-O)_4(Si_8O_{12})Ag]$ were calculated along the high symmetry lines of the square irreducible *Brillouin* zone (IBZ), Scheme 6. Density of states (DOS) and crystal orbital overlap populations (COOP) were obtained by averaging over 210 k-points in the IBZ. Band structures of $^{2}_{\infty}[(-O)_4(Si_8O_{12})Ag_n]$, n = 2, 3, 4, were calculated along the high symmetry elements of the primitive rectangular IBZ, Scheme 6. Densities of states (DOS) and crystal orbital overlap populations (COOP) were obtained by averaging over 196 k-points of the IBZ. The k-point sets of the planar compounds were generated by the geometrical method of Ramirez and Böhm [54] with grid type 1 including

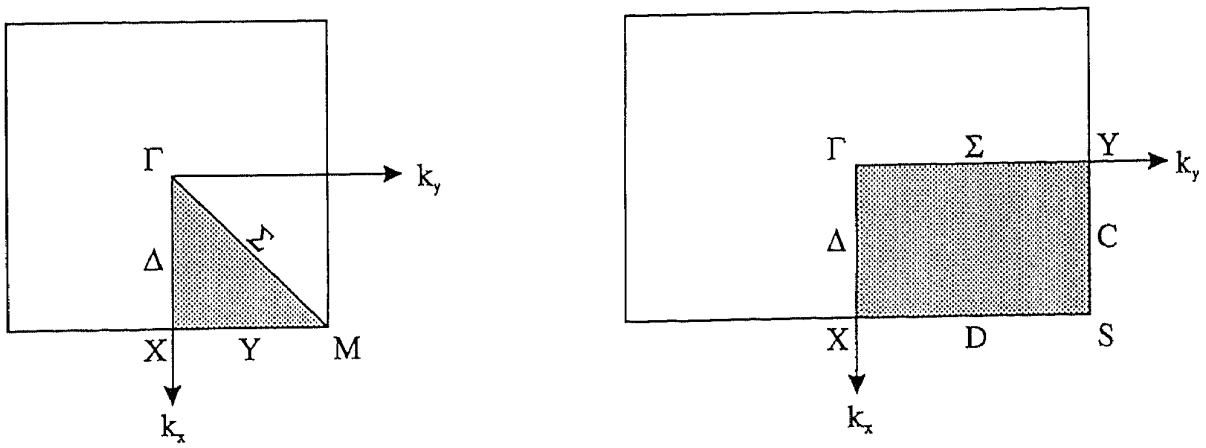

Scheme 6
Square (left) and primitive rectangular (right) irreducible *Brillouin* zone.

the high symmetry k-points. The Bloch sums were running over the next two nearest neighbours. The band structures of the silica zeolite A was calculated along the high symmetry lines of the simple cubic *Brillouin* zone, Scheme 7. The k-point set for the properties calculation was determined by adopting the method described by Macdonald [55]. 165 k-points of the IBZ were taken. In these calculations the Bloch sums ran over one nearest neighbour cell.

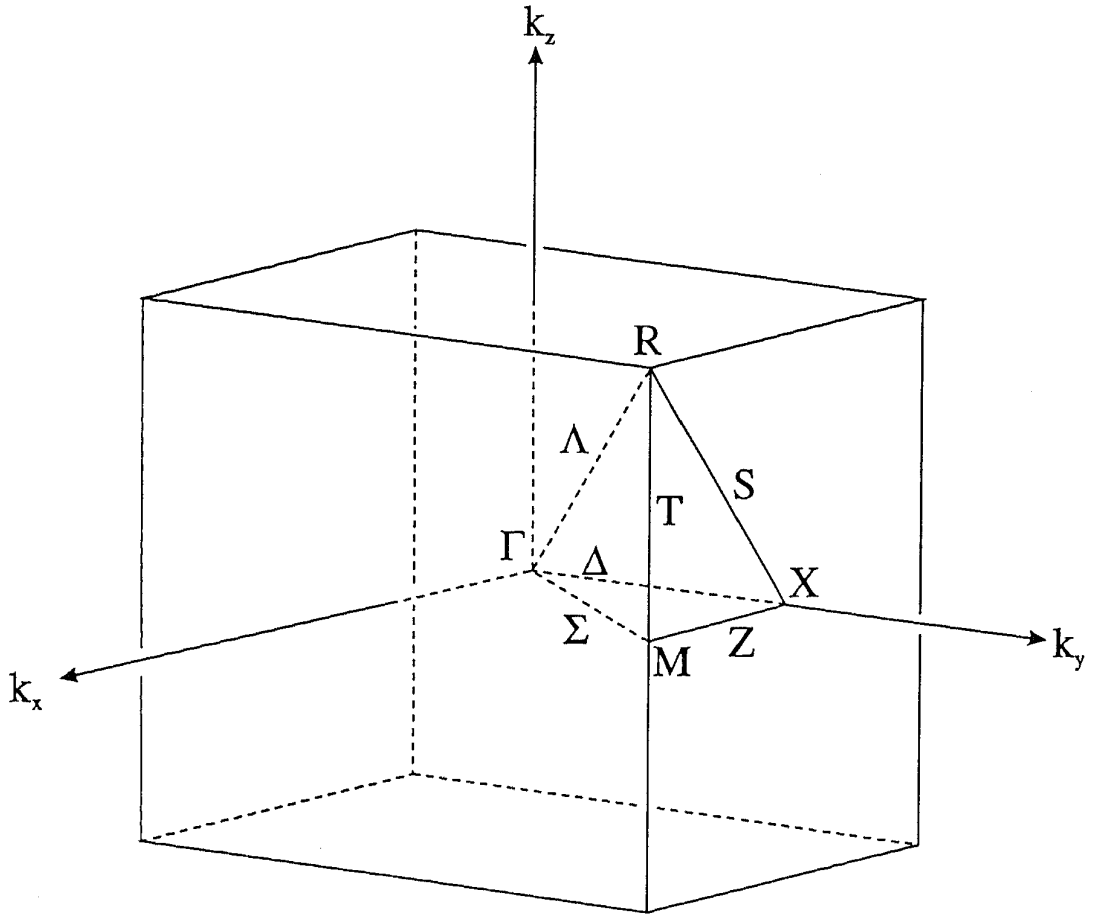

Scheme 7
Simple cubic irreducible *Brillouin* zone.

ELECTRONIC STRUCTURE OF THE $^{2}_{\infty}[(-O)_4(Si_8O_{12})]$ LAYER AND OF THE HIGH-SILICA ZEOLITE A $^{3}_{\infty}[Si_{24}O_{48}]$

Qualitative perturbation theory and extended-Hückel band structure calculations of the two-dimensional $^{2}_{\infty}[Si_2O_5^2]$ frame of phyllosilicates have led to the conclusion that the rotation and tilting of the silicate tetrahedra cause no major changes in the orbital interactions. Both stabilization and destabilization of individual states occur with these distortions, traceable to next-nearest-neighbour oxygen-oxygen interactions. It was shown that the orbital interaction between Si(3s,3p) and O(2s) atomic orbitals in bond formation is important [28]. Most of the results reported in this study are equally valid for the $^{2}_{\infty}[(-O)_4(Si_8O_{12})]$ layer. We focus on the understanding of LMCT states observed in Cu^{+}- and in Ag^{+}-exchanged

zeolites [15,56] and we also take geometry calculations into consideration. The extended-Hückel parameters have been determined accordingly. The different parameters used in our calculations do not affect the conclusions reached in [28], however.

We begin with the band structure of the $^{2}_{\infty}[(\text{-O})_4(Si_8O_{12})]$ layer in Figure 3, calculated

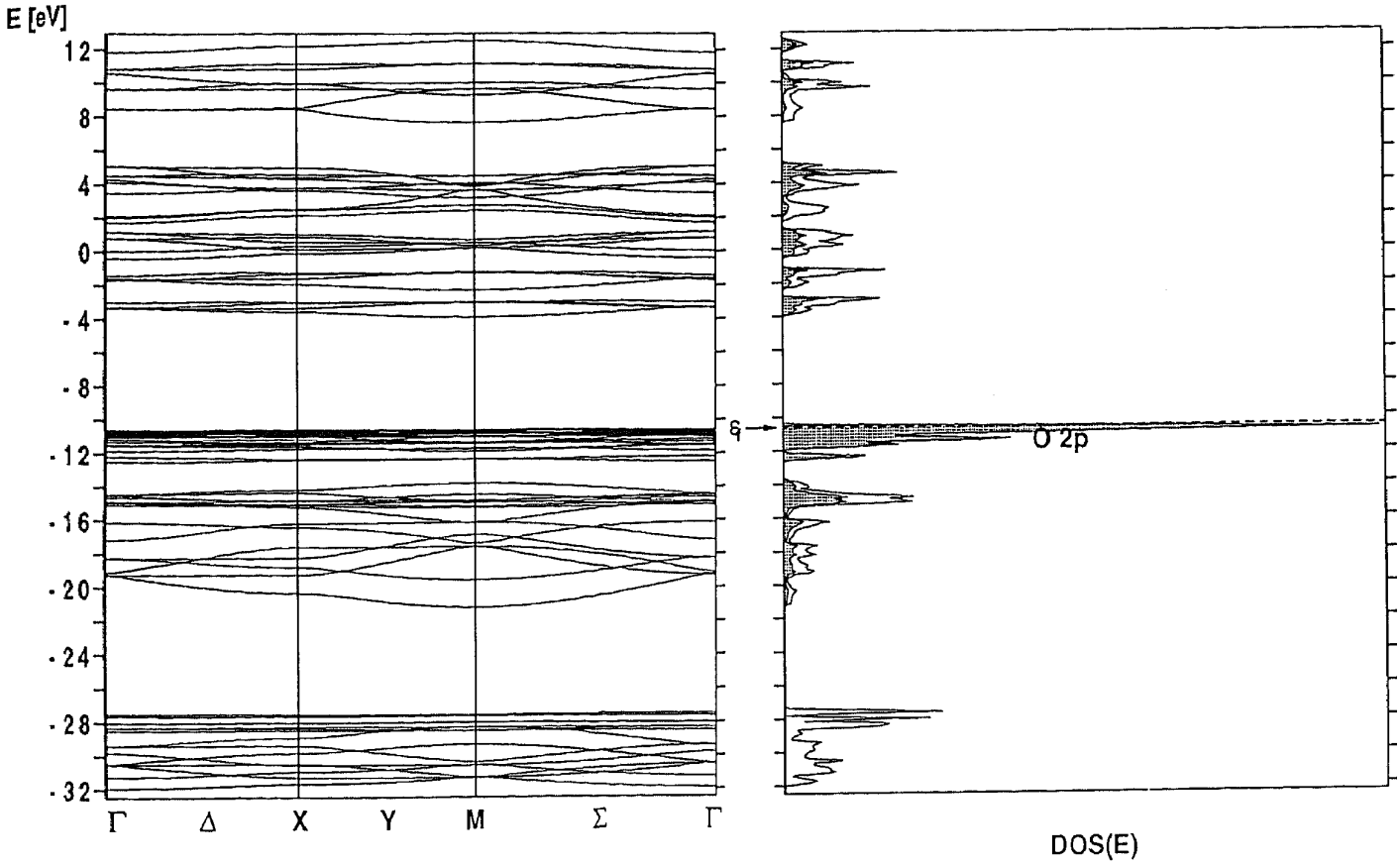

Figure 3. Left: bandstructure of the $^{2}_{\infty}[(\text{-O})_4(Si_8O_2)]$ layer along the high symmetry lines of the square IBZ. Right: corresponding density of states with shaded oxygen 2p density projected out.

along the high symmetry lines of the square IBZ in Scheme 6, and we do not show the computational results obtained for the $^{1}_{\infty}[(\text{-O})_2H_4(Si_8O_{12})]$ chain because they are very similar. It is remarkable how well the general features of this $^{2}_{\infty}[(\text{-O})_4(Si_8O_{12})]$ band structure correspond to the experimentally determined band structure of α-quartz, see Figure 6 of [35]. The calculated Fermi level lies at -10.55 eV, which is close to the experimental α-quartz value of about -10.4 eV and also close to the -10.7 eV observed for octahydrosilasesquioxane $H_8Si_8O_{12}$ [21]. The valence band of α-quartz extends approximately from -10.4 eV to -21 eV followed by a gap of 8 eV after which the 2s oxygen levels are observed. On the other side the LUMO appears at about 9 eV above the Fermi level. If we disregard the smaller density of states of the two-dimensional $^{2}_{\infty}[(\text{-O})_4(Si_8O_{12})]$ we can state that this model represents the main features of the electronic structure of α-quartz.

Based on our knowledge that the highest occupied orbitals of $H_8Si_8O_{12}$ [21] are oxygen lone pairs and based on the studies of the two-dimensional $^{2}_{\infty}[Si_2O_5^{2}]$ phyllosilicate frame [28] we are not astonished to observe that the bands in the HOMO region are flat and

indicate that nonbonding states are involved. Further insight is gained from the density of states DOS(E), defined such that DOS(E)dE is the number of states in the interval E to E+dE. Since we are expressing our crystal orbitals as a linear combination of atomic orbitals (LCAO) we can project out specific atomic orbitals or linear combinations of atomic orbitals [25,46]. In Figure 3 this has been done by shading the oxygen 2p contribution and leaving the 2s oxygen and the silicon contributions blank. This projection shows that the HOMO region consists of nearly pure oxygen 2p lone pairs which we denote as (| O<) [13,15,56]. Some bands below -14 eV are significantly bent and contribute to the Si-O bonding.

The band structure and the DOS of the silica zeolite A in Figure 4 exhibits the same

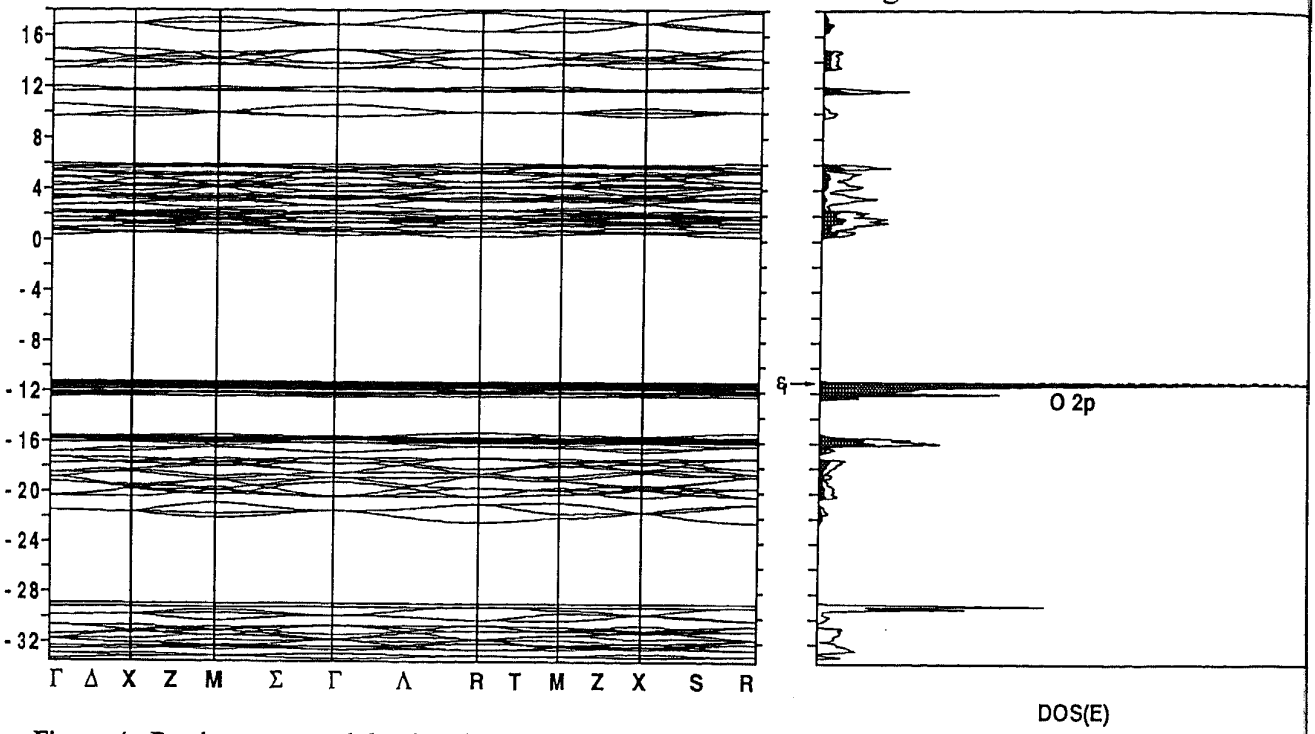

Figure 4. Band structure and density of states of the silicon dioxide analogue of zeolite A. Scheme 4. The oxygen 2p density is projected out.

features as already encountered in the $^{2}_{\infty}[(\text{-O})_4(Si_8O_{12})]$ layer. This means that this two-dimensional network, and even the linear chain, already reflect the main features of the three-dimensional extended structure of the silica zeolite A. This is the typical behaviour expected for an insulator with saturated valencies whose electronic structure can be described as being localized and is already present in the starting $H_8Si_8O_{12}$ molecule. It also explains the finding that this molecule is an excellent starting point for the description of the vibrational structure of zeolite A [34].

PLACING SILVER ATOMS INTO THE D8R CAVITIES

We begin by putting one silver atom into the centre of each of the 4.1 Å diameter D8R cavities, Scheme 8. The silver atoms form a square layer of 7.523 Å unit cell length and

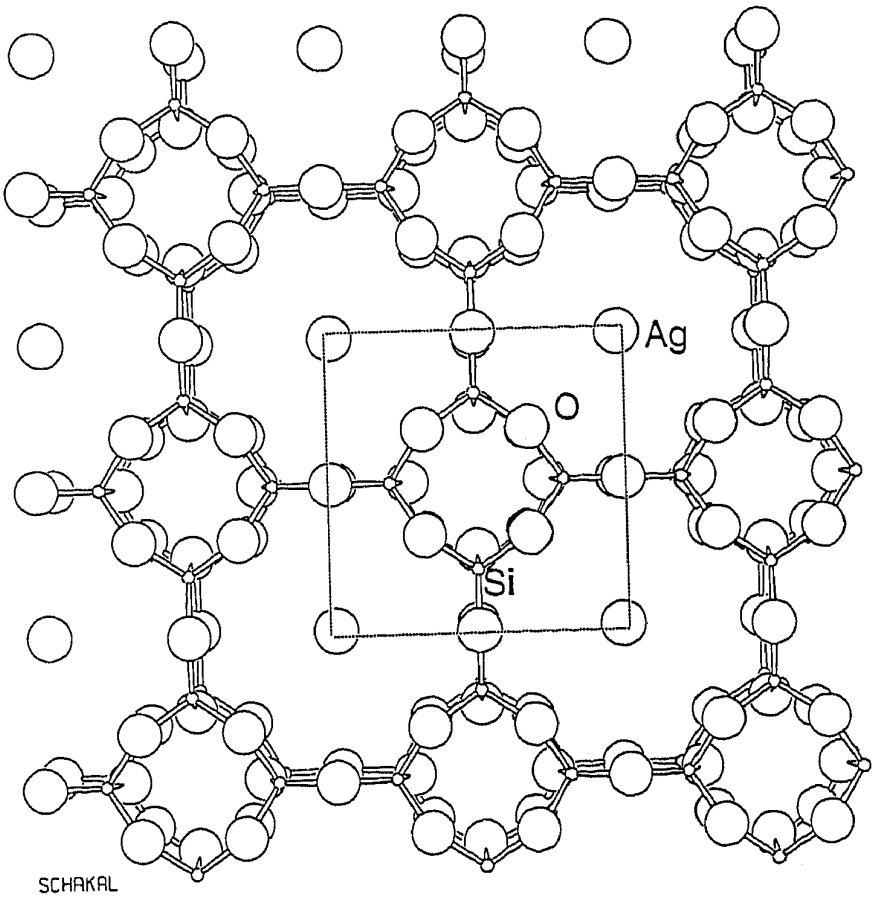

Scheme 8
$^{2}_{\infty}[(-O)_4(Si_8O_{12})Ag]$ layer.

p4mm symmetry. Next we move the silver atoms in the direction of the Si_4O_4 rings vertical to the plane of the $^{2}_{\infty}[(-O)_4(Si_8O_{12})]$ layer to trace their interaction with the zeolitic framework. This allows us to proceed to linear Ag chains with alternating Ag-Ag distances by adding a second silver atom. The Ag-O distances of this p2mm network, illustrated in Scheme 9, were estimated from ionic and atomic radii [57,58] and correspond to experimental values reported for silver zeolite A [3,4]. Let us remark that these are purely hypothetical arrangements, useful to learn how the electronic structure develops.

A further silver atom per D8R can be added by capping the Ag_2 chains from above. The distance between the capping Ag and an Ag in the centre plane is 2.89 Å and corresponds to the bulk metal distance. The filling capacity of the D8R cavities is reached when putting the fourth Ag in the same way as before from below resulting in the p2mm layer in Scheme 10. The rhombohedral Ag_4 clusters in the D8R have a structure similar to the Jahn-Teller distorted free Ag_4 [13].

The band structures of the thus generated $^{2}_{\infty}[(-O)_4(Si_8O_{12})Ag_n]$, n = 1,2,3,4, layers are shown in Figure 5. In the first case with one Ag per D8R, Scheme 8, the band structure is simply a superposition between that of the silicon dioxide layer $^{2}_{\infty}[(-O)_4(Si_8O_{12}]$, Figure 3, and that of the 5s and 4d levels of a layer of nearly non-interacting silver atoms. Only the 5p levels are slightly perturbed because the Ag-5p atomic orbitals are very diffuse and

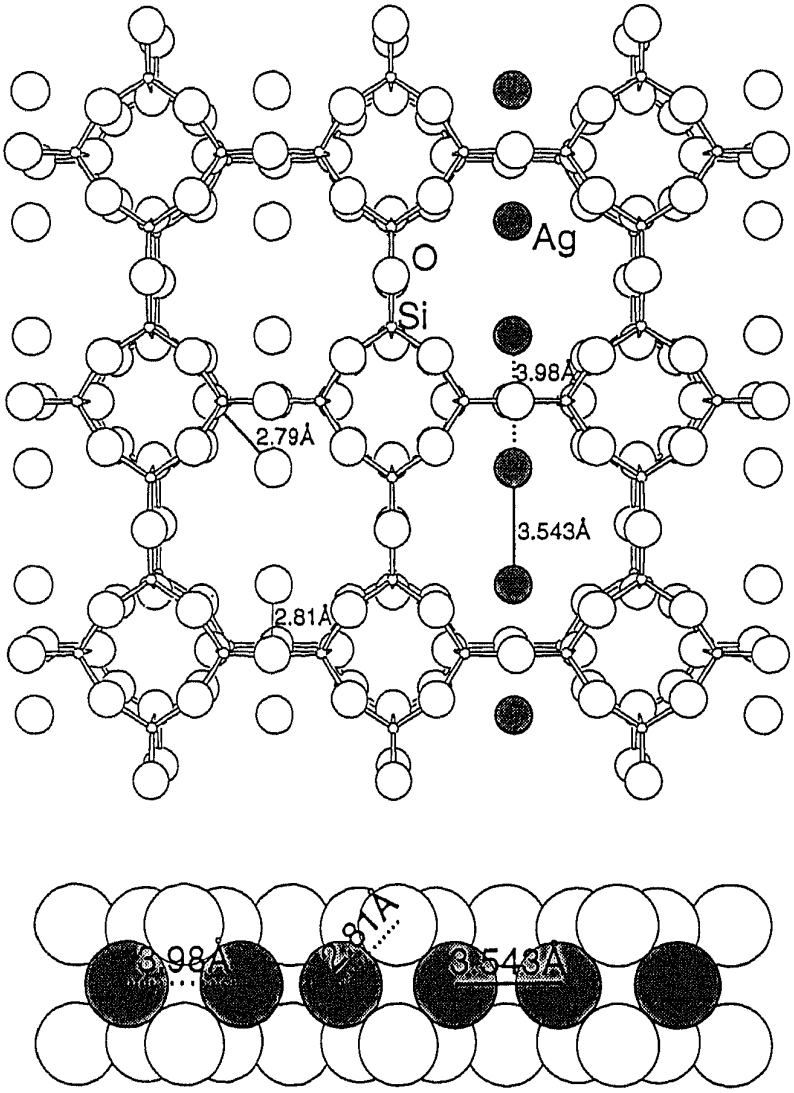

Scheme 9
$^{2}_{\infty}[(\text{-O})_4(Si_8O_{12})Ag_2]$ layer.

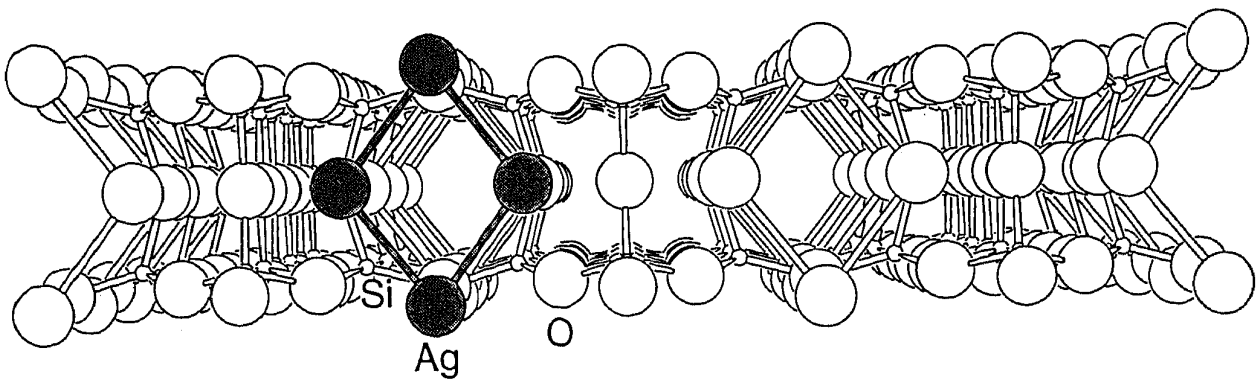

Scheme 10
$^{2}_{\infty}[(\text{-O})_4(Si_8O_{12})Ag_4]$ layer.

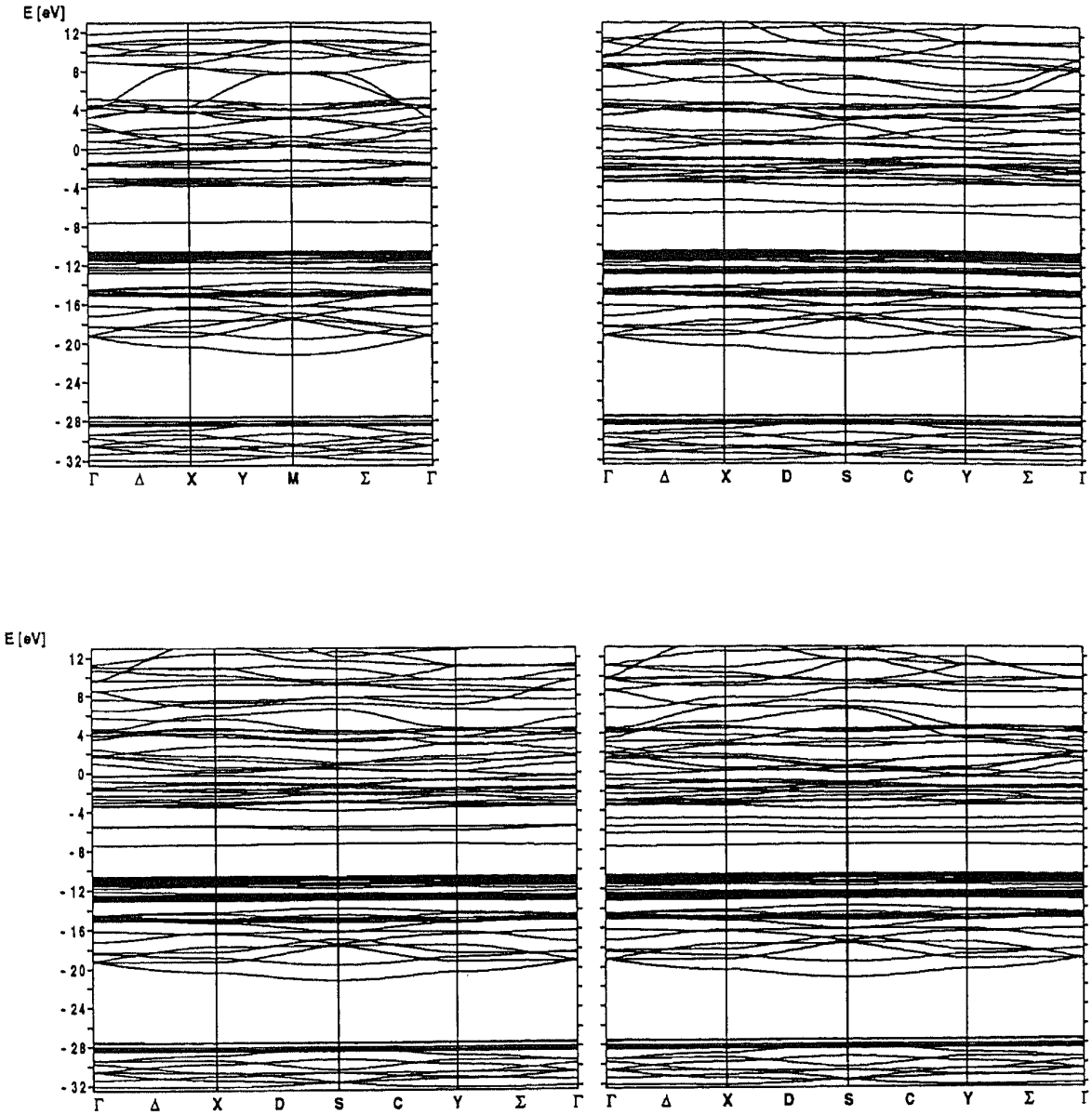

Figure 5. Band structure diagrams of the $^{2}_{\infty}[(\text{-O})_4(Si_8O_{12})Ag_n]$ layers. Upper left, n = 1; upper right, n = 2; lower left n = 3; lower right n = 4.

can interact over very long distances. We conclude that the simple diagram in Figure 1 describes this situation quite well. Moving the silver atoms from the centre to the Si_4O_4 rings vertical to the plane of the $^{2}_{\infty}[(\text{-O})_4(Si_8O_{12})]$ layer causes the antibonding interaction between the 5s band of the Ag and the oxygen lone pairs denoted as Δ in Figure 1. The destabilizing three-electron interaction between the double occupied oxygen levels and the single occupied silver level is illustrated in Figure 9b which explains the mixing of the O-2p and the Ag-5s densities and which will be discussed later in more detail. The energy position of the Ag-5s band depends on two parameters, one is the Coulomb integral of the Ag, H_{5s5s}, and the other one is the Ag-O distance. Both are subject to some uncertainty but there is no doubt that the first electronic transition observed in a $^{2}_{\infty}[(\text{-O})_4(Si_8O_{12})Ag^{m+}]$, m

= 0,1, layer is of oxygen to silver charge transfer type, denoted as $Ag^{m+} \leftarrow (|O<)$ LMCT (ligand to metal charge transfer), and has an energy in the order of 3 eV, see also [15]. The DOS and COOP plots in Figure 6 give some further information. First we recognize

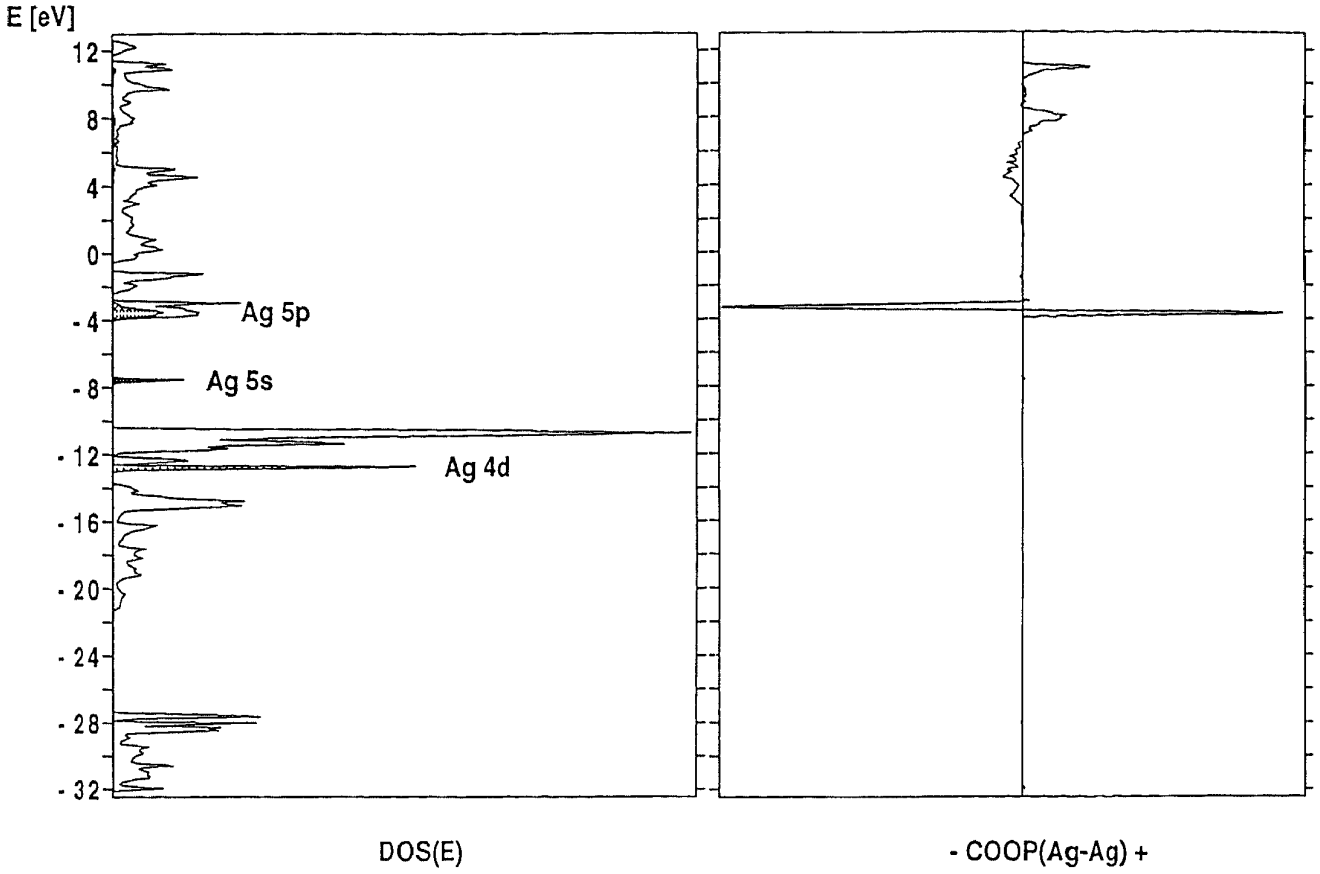

Figure 6. Left: density of states of $^2_\infty[(-O)_4(Si_8O_{12})Ag]$. The shaded regions are the separately projected out Ag densities. Right: corresponding crystal orbital overlap population denoting the antibonding/bonding (-/+) Ag-Ag interaction ($d_{Ag\text{-}Ag}$ = 7.523 Å).

that the Ag-4d and the Ag-5s densities are well isolated from those of the silicon dioxide framework and that only the high lying Ag-5p show some interaction with the antibonding SiO_2 states, pushing some bands to higher energy. The transition of an electron from the O-2p lone pair band to the Ag-5s band in the LMCT excitation is nicely illustrated by this DOS diagram. To what extent the silver atoms "feel" each other across the layer can be traced by the crystal orbital overlap population (COOP). A very small dip, barely visible, at the 5s level energy indicates a tiny overlap between the Ag-5s orbitals. The amount of this overlap depends on the diffuseness of the Ag-5s orbitals and can therefore be influenced in the calculations to some extent by tuning the 5s Slater exponent. This is easily recognized by looking at the Ag-5p region. The 5p orbitals are much more diffuse than the 5s ones, see Table 1, and hence the COOPs, bonding and antibonding, are much larger while the COOP vanishes for the more contracted 4d orbitals. Since mainly the 5s orbitals are more contracted for Ag^+ than for Ag^0 the electronic Ag-Ag interaction is larger in the fully reduced lattice than in the oxidized one.

We now proceed to the band structure of $^2_\infty[(-O)_4(Si_8O_{12})Ag_2]$ on the top of Figure 5,

right. In this diagram the Ag-O distance is smaller than in the former case and hence the Ag-5s bands are pushed to higher energy. Interaction between the silver atoms causes splitting of all Ag bands. We focus on the Ag-5s bands which are of main interest to us. According to Figure 9, c and d, the formation of two bands is expected, the 5σ originating from the 5s+5s bonding interaction between the two silver atoms in each cage and the $5\sigma^*$ from the 5s-5s antibonding interaction. The splitting of the two bands amounts to approximately 1.37 eV at the Γ-point and to 0.73 eV at the Y-point, and the band width, which represents the electronic coupling between the Ag_2 in the different cages is about 0.27 eV and 0.43 eV in the case of 5σ and $5\sigma^*$, respectively. The largest band dispersions are observed along the alternating Ag-Ag distances, described by the ∑ and D lines, while the flat bands along Δ and C indicate nearly vanishing coupling of the silver chains.

We can still try to describe the band structure in a first order approximation as superposition between the bands of the $^2_\infty[(\text{-O})_4(Si_8O_{12})]$ framework and the bands of a hypothetical $^2_\infty[Ag_2]$ layer in Figure 7. Intercalation of the silver chains into the framework

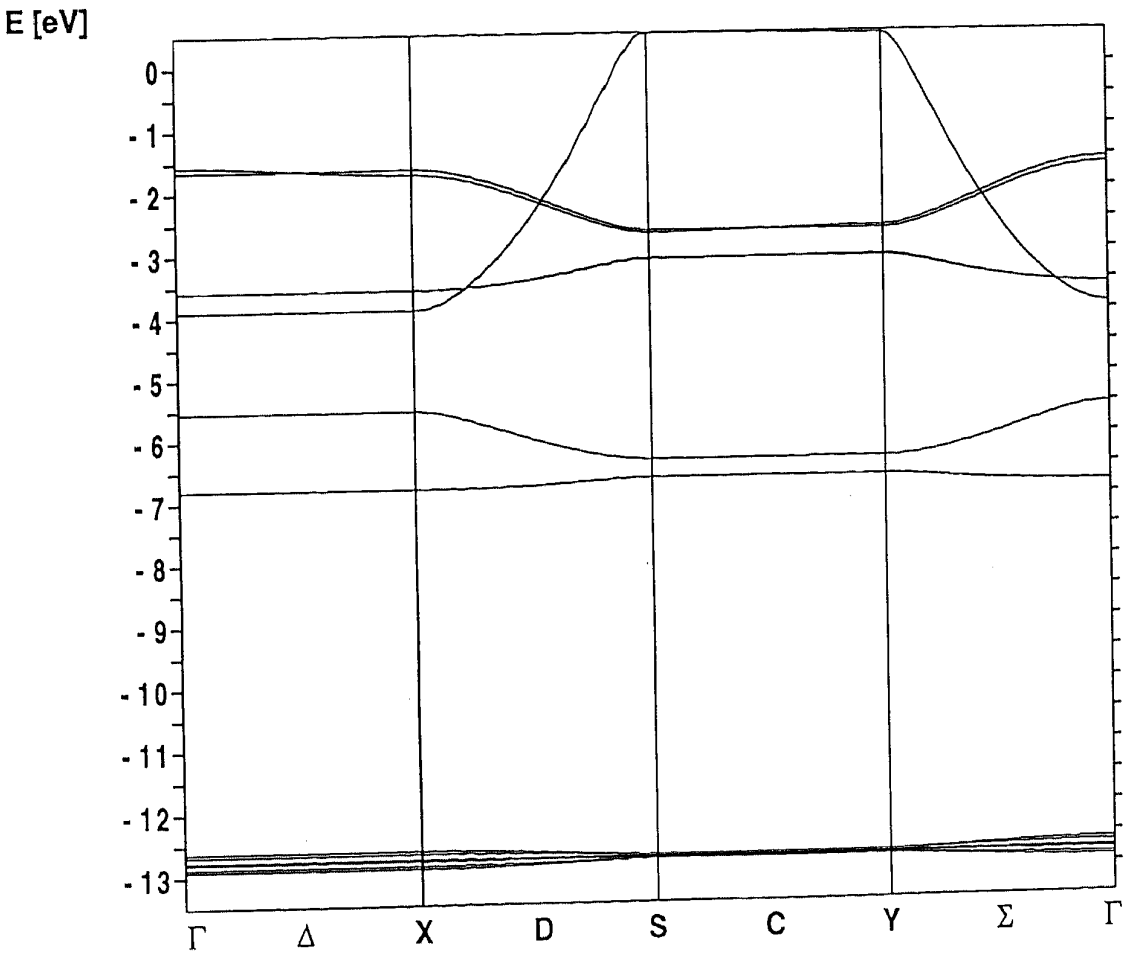

Figure 7. Band structure of a $^2_\infty[Ag_2]$ layer with the same geometry as the Ag chains in Scheme 9. The 5σ and $5\sigma^*$ bands lie between -7 and -5 eV.

causes, however, significant changes. The separation into Ag_2 clusters, already favoured by the Peierls distortion of the free non-alternating Ag-chain, is enhanced by antibonding

Ag-O interactions. The bonding of the silver atoms within the D8R gets stronger, as can be seen from the broadening of the band width of the 5σ band along the D line, X to S, in Figure 5, upper right, compared to Figure 7, whereas the dispersion of the $5\sigma^*$ band expressing the antibonding interaction of the Ag atoms within the D8R is diminished. In any case the coupling of the Ag_2 visualized by the dotted line in the COOP plot in Figure 8 remains weak enough so that it makes sense to describe the individual Ag_2 within the

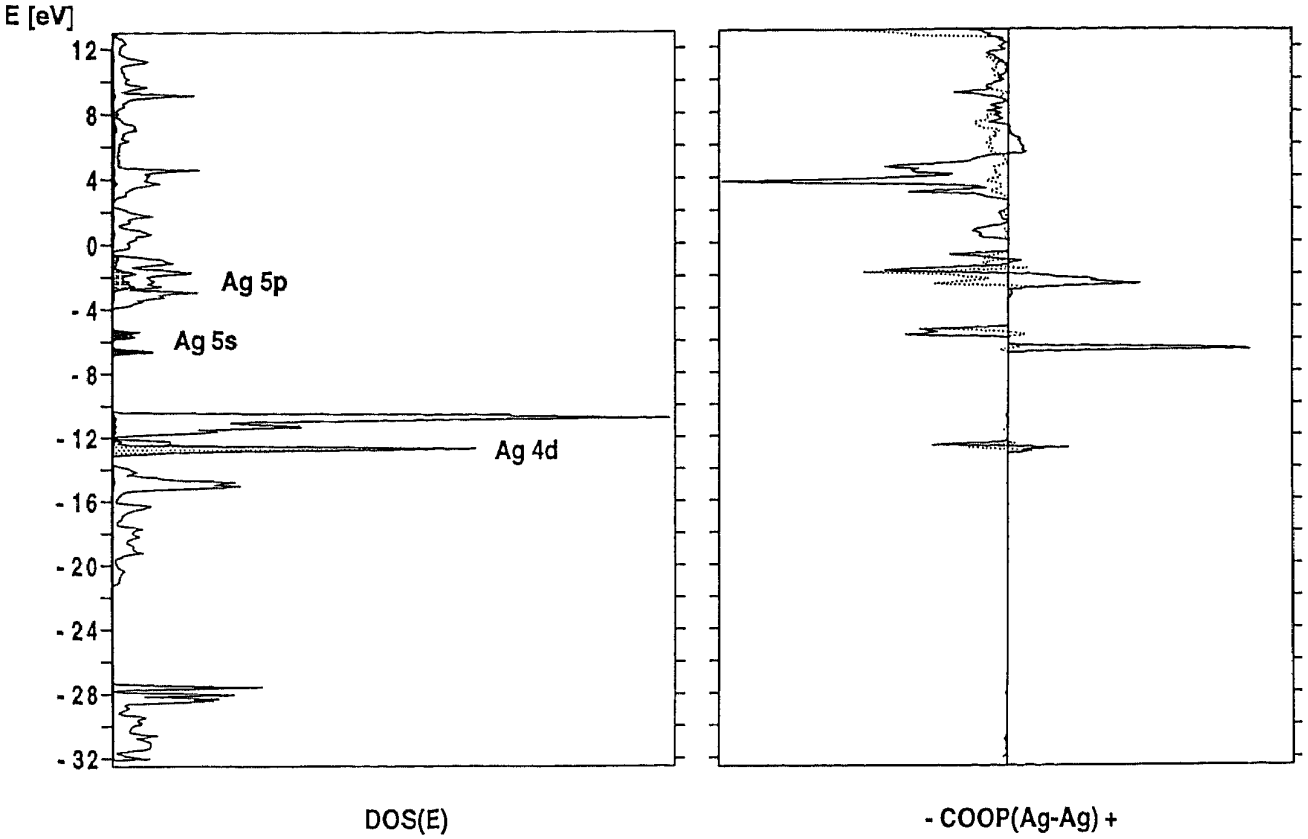

Figure 8. Left: density of states of $^2_\infty[(\text{-O})_4(Si_8O_{12})Ag_2]$. The shaded regions are the separately projected out Ag densities. Right: corresponding Ag-Ag crystal orbital overlap population. ———: $d_{Ag\text{-}Ag} = 3.543$ Å, within the D8R; - - - - -: $d_{Ag\text{-}Ag} = 3.98$ Å, to next neighbour cell.

D8R as quantum dots weakly interacting with each other along the chains. The disturbance by the Ag-O interaction is again most pronounced in the Ag-5p region, as best recognized by looking at the DOS and the COOP in Figure 8. But there is some Ag-5s density in the oxygen lone pair region and we can try the hypothesis that this density can assist hole hopping along the zeolite framework after LMCT photoexcitation. We also observe that the energy difference between the zeolite HOCO (highest occupied crystal orbital) and the 5σ band is reduced with respect to the $^2_\infty[(\text{-O})_4(Si_8O_{12})Ag^{m+}]$, m = 0,1, layer, because of the 5σ, $5\sigma^*$ splitting. The still narrow Ag-4d band has broadened due to the number of d orbitals and the shorter Ag-Ag distances. We should add that the distance d(Ag-Ag) in a fully oxidized D8R-cage containing two Ag^+ is dominated by their *Coulomb* repulsion. If one of them is reduced bonding interactions occur and hence the distance d(Ag-Ad) becomes smaller and the 5σ,$5\sigma^*$ splitting increases. This mechanism accounts for the bathochromic shift of the spectral sensitivity in the early stage of the photochemical

oxidation of water with silver zeolites, called self-sensitization [5,6].

We have already made reference to the fragment MO analyses in Figure 9 in which the $^{2}_{\infty}[(\text{-O})_4(Si_8O_{12})]$ layer is first broken into small siloxane fragments, a. Next, b, we show the interaction of an Ag-5s orbital with the framework oxygens of the Si_4O_4 rings vertical to the plane of the $^{2}_{\infty}[(\text{-O})_4(Si_8O_{12})]$ layer. It is repulsive and destabilizes the Ag-5s band, now called 5s' as in Figure 1, and slightly stabilizes the oxygen lone pair levels. By this

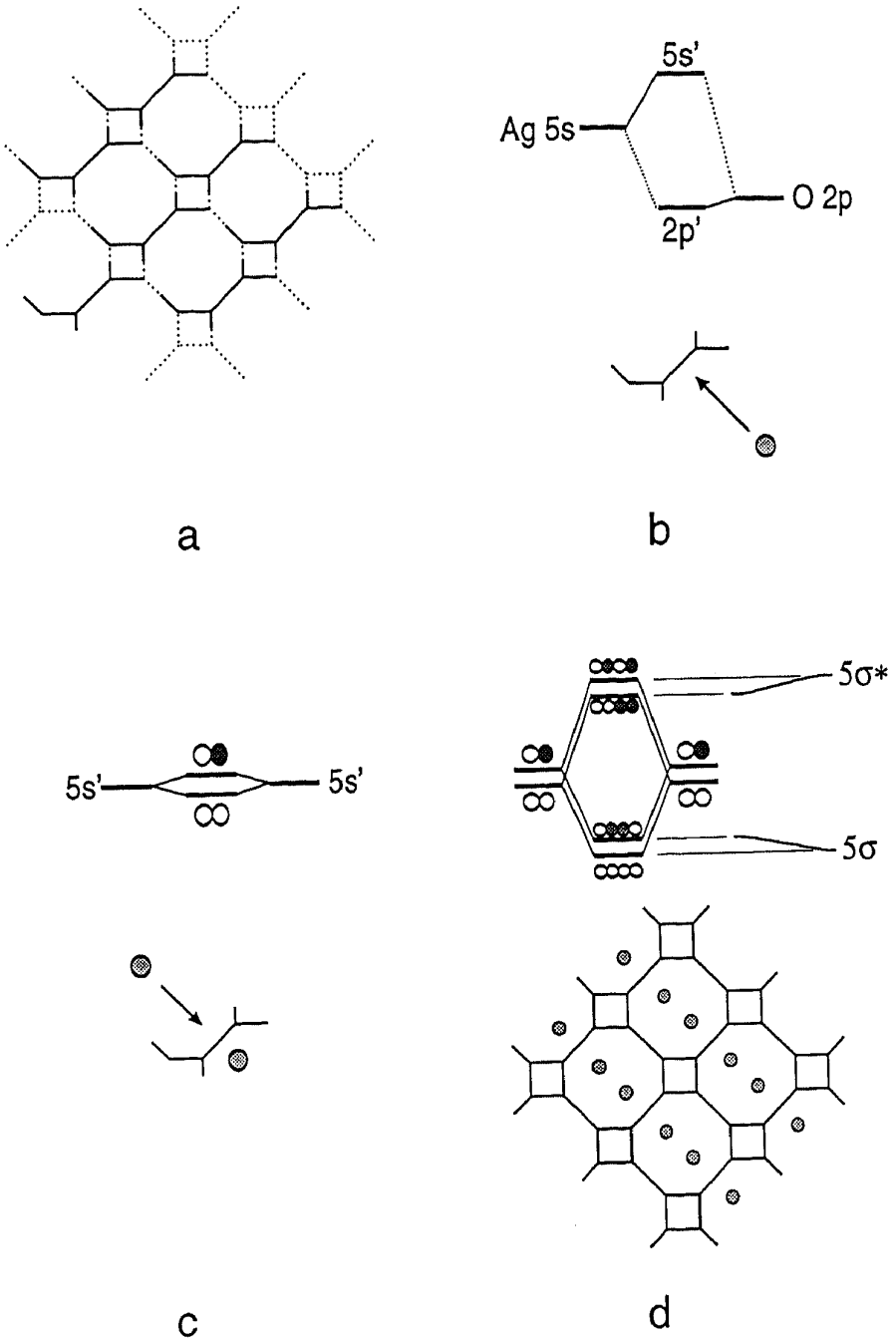

Figure 9. Molecular orbital diagram explaining the Ag-Ag and the Ag-O interactions in $^{2}_{\infty}[(\text{-O})_4(Si_8O_{12})Ag_2]$ layers. a: The $^{2}_{\infty}[(\text{-O})_4(Si_8O_{12})]$ layer is broken into small siloxane fragments. b: Interaction between an Ag-5s orbital and the framework oxygens of the Si_4O_4 rings vertical to the plane of the $^{2}_{\infty}[(\text{-O})_4(Si_8O_{12})]$ layer. c: Weak interaction with an Ag approaching from the opposite side. d: Reconnection of the fragments. The silver levels evolve into bands.

interaction some density of both levels mixes into each other. In the third step, c, a second silver atom approaches from the opposite side. Its interaction with the Ag on the other side of the Si_4O_4 results in a small bonding and antibonding splitting of the Ag-5s. When in a last step, d, these fragments are reconnected the final 5σ and $5\sigma^*$ bands evolve as indicated. The bonding and antibonding character of these bands is visualized in the Ag-Ag COOP in Figure 8. From this analysis it is evident that none of the $^2_\infty[(\text{-O})_4(Si_8O_{12})Ag_n]$, n = 1,2,3,4, layers are stable in their reduced form. Silver would migrate to the surface of the layer and form bulk silver. Stabilization would either demand cage structures with small pore openings to prevent transport of Ag and/or a cationic framework, compensated by negatively charged $[AlO_2]^-$ units, as encountered in Ag-A zeolites [16,17]. The same conclusion, which is not astonishing, has already been reached in earlier studies [20]. We do, however, expect that the $[AlO_2]^-$ units, although necessary for stability, have not too much influence on the electronic structure so that our arguments remain valid in aluminosilicates as well, a conclusion that was also reached in an molecular orbital study of phyllosilicates [28].

The evolution of the bands if one goes to higher silver loading does not bring many surprises. For Ag_3, Figure 5 lower left, and Ag_4, Figure 5 lower right, the bands evolve in the expected way. The energy range occupied by the 5s bands expands and hence the energy difference between the zeolite HOCO and the lowest Ag-5s band is reduced. The 4d band width increases and the DOS of the d bands becomes large. It would be interesting to know how the overlap of the oxygen nonbonding states and the silver 4d states evolve if the clusters are allowed to grow and we are wondering about electronic long range coupling. With this and other questions we reach the limit of the $^2_\infty[(\text{-O})_4(Si_8O_{12})Ag_n]$, n = 1,2,3,4, framework and calculations on zeolite A loaded with octahedral Ag_6 clusters in the α- or in the β-cage, illustrated in Figure 10, are needed to go a further step.

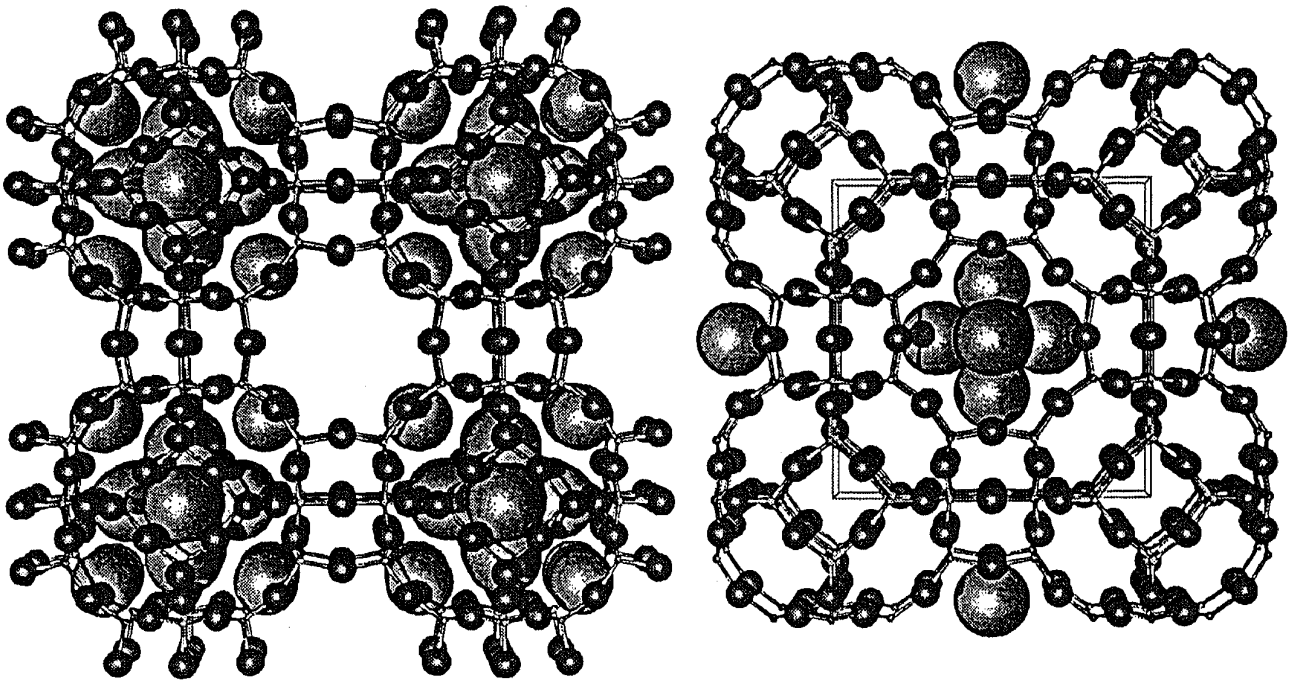

Figure 10. Ag_6 clusters in the α-cage (left) and in the sodalite cage (right) in zeolite A, as determined by X-ray structure [3-4].

Acknowledgement

The calculations were performed on an IBM RS/6000 workstation provided by IBM Corporation on terms of a Joint Study Agreement. We would like to than Dr. Konrad Hädener for his contributions in the preliminary stage of this work and we gratefully acknowledge support by the Schweizerische Bundesamt für Energiewirtschaft (BEW-REN(88)28/EPA 217.307) and by the Schweizerische Nationalfonds zur Förderung der wissenschaftlichen Forschung grant No. 20-28528.90.

REFERENCES

1. H.K. Beyer and P.A. Jacobs, In: Metal Microstructures in Zeolites, P.A. Jacobs (Ed.), pp. 95-102, Elsevier Scientific, Amsterdam, 1982.
2. G. Calzaferri, W. Suter, and B. Waldeck, J. Chem. Soc. Chem. Commun. 485 (1990).
3. S.H. Song, Y. Kim, and K. Seff, J. Phys. Chem. **95**, 9919 (1991).
4. a) Y. Kim and K. Seff, J. Am. Chem. Soc. **100**, 6989 (1978); b) Y. Kim and K. Seff, J. Phys. Chem. **82**, 1307 (1978).
5. G. Calzaferri, S. Hug, T. Hugentobler, and B. Sulzberger, J. Photochem. **26**, 109 (1984).
6. R. Beer, F. Binder, and G. Calzaferri, J. Photochem. Photobiol. A: Chem. **69**, 67 (1992).
7. J. Li and G. Calzaferri, J. Chem. Soc. Chem. Commun. 430 (1993).
8. P. Mulvaney and A. Henglein, J. Phys. Chem. **94**, 4182 (1990).
9. P. Mulvaney and A. Henglein, Chem. Phys. Lett. **168**, 391 (1990).
10. P.Y. Cheng and M.A. Duncan, Chem. Phys. Lett. **152**, 341 (1988).
11. W. Harbich, S. Fedrigo, and J. Buttet, Chem. Phys. Lett. **195**, 613 (1992).
12. G.A. Ozin, A. Kuperman, and A. Stein, Angew. Chem. **101**, 373 (1989).
13. G. Calzaferri, In: Photochemical and Photoelectrochemical Conversion and Storage of Solar Energy, Proceedings IPS-9, August 23-29, 1992, Beijing, China, Z.W. Tian and Y. Cao (Eds.), p. 141-157, International Academic Publisher, 1993. In Table 1, p. 152, C2 should read 0.329.
14. B. Sulzberger and G. Calzaferri, J. Photochem. **19**, 321 (1982).
15. R. Beer, G. Calzaferri, J. Li, and B. Waldeck, Coord. Chem. Rev. **111**, 193 (1991).
16. Y. Kim and K. Seff, J. Am. Chem. Soc. **99**, 7055 (1977).
17. Y. Kim and K. Seff, J. Phys. Chem. **91**, 668 (1987).
18. J.R. Morton and K.F. Preston, J. Mag. Reson. **68**, 121 (1986).
19. J.R. Morton and K.F. Preston, Zeolites **7**, 2 (1987).
20. a) G. Calzaferri and L. Forss, Helv. Chim. Acta **69**, 873 (1986); b) *Ibid.*, **70**, 465 (1987).
21. G. Calzaferri and R. Hoffmann, J. Chem. Soc. Dalton Trans. 917 (1991).
22. G.A. Ozin, F. Hugues, and S.M. Mattar, J. Phys. Chem. **89**, 300 (1985).
23. K. Narita, J. Luminescence **4**, 73 (1971).
24. A. Henglein, Ber. Bunsenges. Phys. Chem. **94**, 600 (1990).
25. S. Ciraci and I.P. Batra, Phys. Rev. **B15**, 4923 (1977).
26. A. Breeze and P.G. Perkins, J. Chem. Soc. Farad. Trans. II. **69**, 1237 (1973).
27. A.C. Hess and V.R. Saunders, J. Phys. Chem. **96**, 4367 (1992).
28. W.F. Bleam and R. Hoffmann, Phys. Chem. Minerals **15**, 398 (1988).
29. J.C. White, J.L. Anchell and A.C. Hess, Zeolite '93, 4th International Conference on the Occurence, Properties and Utilization of Natural Zeolites, Program and Abstracts, Idaho, (1993).
30. L.R. Gellens, W.J. Mortier, R. Lissilour and A. Le Beuze, J. Phys. Chem. **86**, 2509 (1982).
31. a) A. Stein, G.A. Ozin, P.M. Macdonald, G.D. Stucky, and R. Jelinek, J. Am. Chem. Soc. **114**, 5171 (1992); b) A. Stein, G.A. Ozin, and G.D. Stucky, J. Am. Chem. Soc. **114**, 8119 (1992).

32. a) W.M. Meier and D.H. Olson, Atlas of Zeolite Structure Types, 2nd Ed., Butterworths, London (1987); b) D.W. Breck, Zeolite Molecular Sieves, John Wiley & Sons, New York, 1974.
33. G. Calzaferri, Nachr. Chem. Tech. Lab. **40**, 1106 (1992).
34. M. Bärtsch, P. Bornhauser, G. Calzaferri, and R. Imhof, submitted for publication.
35. D.L. Griscom, J. Non-Cryst. Solids **24**, 155 (1977).
36. T.P.E. Auf der Hyde, H.-B. Bürgi, H. Bürgy, and K.W. Törnroos, Chimia **45**, 38 (1991).
37. a) P. Bornhauser and G. Calzaferri, Spectrochimica Acta **46A**, 1045 (1990); b) M. Bärtsch, P. Bornhauser, H. Bürgy, and G. Calzaferri, Spectrochimica Acta **47A**, 1627 (1991).
38. H.-B. Bürgi, K.W. Törnroos, G. Calzaferri, and H. Bürgy, Inorg. Chem. (1993), in press.
39. G.V. Gibbs, M.M. Hamil, S.J. Louisnathan, L.S. Bartell, and H. Yow, Am. Mineral **57**, 1578, 1614 and 1643 (1972).
40. G. Calzaferri, R. Imhof, and K.W. Törnroos, J. Chem. Soc., Dalton Trans. (1993), in press.
41. R. Hoffman, J. Chem. Phys. **39**, 1397 (1963).
42. G. Calzaferri, L. Forss, and I. Kamber, J. Phys. Chem. **93**, 5366 (1989).
43. a) M. Brändle and G. Calzaferri, Helv. Chem. Acta **76**, 924 (1993); b) F. Savary, J. Weber, and G. Calzaferri, J. Phys. Chem. **97**, 3722 (1993).
44. G. Calzaferri and M. Brändle, ICONC & INPUTC, Quantum Chemistry Program Exchange, QCPE program QCMP #116, OCPE Bulletin **12**, (1992), update May 1993.
45. M.-H. Whangbo and R. Hoffmann, J. Am. Chem. Soc. **100**, 6093 (1978).
46. R. Hoffmann, Solids and Surfaces, A Chemist's View of Bonding in Extended Structures, VCH Publishers, Inc., 22 East 23rd St., Suite 909, New York 10010 (1988).
47. M. Brändle and G. Calzaferri, Helv. Chim. Acta **76**, 2350 (1993).
48. M.-H. Whangbo, M. Evain, T. Hughbanks, M. Kertesz, S. Wijeysekera, C. Wilker, and R. Hoffmann, EHMACC - Extended-Hückel Molecular, Crystal and Properties Package, QCPE program QCPE #571, OCPE Bulletin **9**, (1989).
49. a) A.C. Hess, P.F. McMillan, and M. O'Keeffe, J. Phys. Chem. **92**, 1785 (1988); b) A.C. Hess, P.F. McMillan, and M. O'Keeffe, J. Phys. Chem. **91**, 1395 (1987).
50. J. Sauer, Chem. Phys. Letters **97**, 275 (1983).
51. a) G.V. Gibbs, P. D'Arco, and M.B. Boisen, Jr., J. Phys. Chem. **91**, 5347 (1987); b) G.V. Gibbs, Am. Mineral **67**, 421 (1982).
52. D.M. Bibby and M.P. Dale, Nature **317** 157 (1985).
53. J.W. Richardson, Jr., J.J. Pluth, J.V. Smith, W.J. Dytrych, and D.M. Bibby, J. Phys. Chem. **92**, 243 (1988).
54. R. Ramfrez and M.C. Böhm, Int. J. Quant. Chem. **30**, 391 (1986).
55. a) A.H. MacDonald, Phys. Rev. **B18**, 5897 (1978); b) M. Lax, Symmetry Principles in Solid State and Molecular Physics, John Wiley & Sons, New York (1974); c) C.J. Bradley and A.P. Cracknell, The Mathematical Theory of Symmetry in Solids, Clarendon Press, Oxford (1972); d) J.F. Cornwell, Group Theory in Physics, Vol. I, Academic Press, London, 1984.
56. G. Calzaferri, R. Giovanoli, I. Kamber, V. Shklover, and R. Nesper, Research on Chemical Intermediates **19**, 31 (1993).
57. Gmelins Handbuch der Anorganischen Chemie **3**, 8th Ed., Verlag Chemie, Weinheim, 1958.
58. Gmelins Handbuch der Anorganischen Chemie **61 A2**, 8th Ed., Verlag Chemie, Weinheim, 1972.
59. E. Keller, Schakal 88B - a Fortran program for the graphic respresentation of molecular and crystallographic models, Kristallographisches Kristiful der Albert-Ludwigs-Universtitat Freibrug, Germany, 1988. Figure 10 and Schemes 2-5 and 8-10 have been made by means of Schakal 88b.